

# Terahertz-frequency electronic transport in graphene

N. Sule,<sup>\*</sup> K. J. Willis,<sup>†</sup> S. C. Hagness, and I. Knezevic<sup>‡</sup>

*Department of Electrical and Computer Engineering, University of Wisconsin-Madison, Madison, Wisconsin 53706, USA*

(Received 2 June 2014; revised manuscript received 17 July 2014; published 31 July 2014)

We calculate the room-temperature complex conductivity  $\sigma(\omega)$  of suspended and supported graphene at terahertz frequencies (100 GHz–10 THz) by employing a self-consistent coupled simulation of carrier transport and electrodynamics. We consider a wide range of electron ( $n = 10^{12}$ – $10^{13}$  cm<sup>-2</sup>) and impurity ( $N_i = 8 \times 10^{10}$ – $2 \times 10^{12}$  cm<sup>-2</sup>) densities. For graphene supported on SiO<sub>2</sub>, there is excellent agreement between the calculation with clustered impurities and the experimentally measured  $\sigma(\omega)$ . The choice of substrate (SiO<sub>2</sub> or *h*-BN) is important at frequencies below 4 THz. We show that carrier scattering with substrate phonons governs transport in supported graphene for  $N_i/n < 0.1$ . Electron-impurity interactions dominate for  $N_i/n > 0.1$ , and transport enters the electron-hole puddle regime for  $N_i/n > 0.5$ . The simple Drude model, with an effective scattering rate  $\Gamma$  and Drude weight  $D$  as parameters, fits the calculated  $\sigma(\omega)$  for supported graphene very well, owing to electron-impurity scattering.  $\Gamma$  decreases with increasing  $n$  faster than  $n^{-1/2}$  and is insensitive to electron-electron interaction. Both electron-electron and electron-impurity interactions reduce the Drude weight  $D$ , and its dependence on  $n$  is sublinear.

DOI: [10.1103/PhysRevB.90.045431](https://doi.org/10.1103/PhysRevB.90.045431)

PACS number(s): 72.80.Vp, 78.67.Wj

## I. INTRODUCTION

High carrier mobility [1,2] and tunable carrier density [3,4] are two appealing aspects of graphene for traditional electronic device applications [5–9]. The properties of graphene can be modified by transfer onto different substrates [10–12]. In recent years, considerable attention has been given to the optoelectronic [7], plasmonic [13–17], terahertz (THz) [18,19], and radio-frequency [20] applications of this two-dimensional material.

An important factor in evaluating the potential of graphene for applications in the THz range (100 GHz–10 THz) is its complex conductivity  $\sigma(\omega)$ , where  $\omega$  is the angular frequency of the excitation [21,22]. Several groups have theoretically [22–28] and experimentally [29–35] investigated the frequency-dependent transport in graphene, with theoretical studies mostly focusing on the midinfrared and higher frequencies (>20 THz) [26–28]. In the THz range, intraband transport processes dominate and  $\sigma(\omega)$  has been shown to have a Drude-model-like dependence,  $\sigma(\omega) = iD/\pi(\omega + i\Gamma)$ , from which a Drude weight  $D$  and an effective scattering rate  $\Gamma$  are obtained [31,35]. The Drude weight at 0 K, calculated based on the random phase approximation (RPA) and with electron-electron interaction neglected, is  $D_0 = 2\pi E_F/\hbar$  (in units of e<sup>2</sup>/hs) [22]. However, experiments have revealed values of  $D$  lower than  $D_0$  [31,35], while the theoretical studies that include electron-electron interactions have predicted an enhancement in  $D$  over  $D_0$  [22]. While this discrepancy is believed to arise from extrinsic factors, there is no clear understanding of all the aspects that affect the Drude weight, as few theoretical studies have explicitly considered the role of different substrates, or the effects of density [27,28] and distribution [26] of charged impurities on electronic transport in graphene.

In this paper, we calculate  $\sigma(\omega)$  of graphene in the THz-frequency range and at room temperature by employing a detailed microscopic simulation of electron transport coupled with full-wave electrodynamics. We investigate the role of the substrate, charged impurities, and electron-electron interaction for graphene supported on SiO<sub>2</sub>, *h*-BN, and for suspended graphene. The  $\sigma(\omega)$  is numerically calculated for different values of the carrier density  $n$  and the sheet impurity density  $N_i$ . We obtain  $D$  and  $\Gamma$  by fitting a generalized Drude model to the numerical data [36,37]. We obtain excellent agreement with the experimentally measured real part of  $\sigma(\omega)$  [30,33,38] by assuming a clustered charged-impurity distribution and using only impurity density as a variable parameter. We show that substrate engineering can be effective for improving the THz conductivity of graphene at the lower frequencies in the THz range (<4 THz) and relatively low impurity density ( $N_i/n < 0.1$ ).  $\Gamma$  decreases with increasing electron density when charged impurities govern transport, while it is nearly constant when electron scattering with the substrate optical phonons dominates. We show that in the presence of clustered impurities,  $\Gamma$  does not follow the  $\sim N_i/\sqrt{n}$  dependence that was theoretically predicted for a uniform random impurity distribution [39,40]. Furthermore, both short-range electron-electron and electron-impurity interactions lower  $D$ , which can explain the reduction observed in measurements [31]. Without impurities, the Drude weight of graphene on the *h*-BN substrate is higher than for either suspended samples or those supported on SiO<sub>2</sub>.

This paper is organized as follows. In Sec. II, we describe the geometry and the parameters used in our simulation (Sec. II A) and present an overview of the coupled simulation method used for calculating  $\sigma(\omega)$  (Sec. II B). In Sec. III, we present the results. We discuss the agreement of our simulation with experiment and the influence of clustered impurity distributions (Sec. III A), compare a simple-Drude vs a generalized-Drude fit to the calculated  $\sigma(\omega)$  (Sec. III B), obtain an effective scattering rate and identify the corresponding transport regimes based on the relative impurity density (Sec. III C), and discuss the effects of electron-electron

<sup>\*</sup>sule@wisc.edu

<sup>†</sup>Current address: AWR Corporation, Mequon, Wisconsin 53092, USA.

<sup>‡</sup>knezevic@engr.wisc.edu

and electron-impurity interactions on the Drude weight (Sec. III D). We conclude with Sec. IV.

## II. THE SIMULATION FRAMEWORK

We simulate the room-temperature electron dynamics in supported graphene with charged impurities distributed near the interface between graphene and the substrate, while focusing on the frequency-dependent conductivity in the THz-frequency range. We assume the diffusive transport regime, captured through the Boltzmann transport equation [41–43]. A transverse electromagnetic (TEM) plane wave is used to excite the electronic system.

### A. The simulation domain. Materials parameters

A typical geometry used in experiments consists of exfoliated or chemical vapor deposition (CVD)-grown graphene transferred onto an insulating substrate. The most commonly used insulating substrate is a 300-nm-thick SiO<sub>2</sub> layer on top of a Si wafer. In the back of the Si wafer is a gate, used to tune the carrier density in the graphene layer. In our simulation, we assume that the carrier density is tuned by shifting the Fermi level in graphene and we do not explicitly include the Si wafer. The electron density at a given Fermi level is given by  $n = n_1 \mathcal{F}_1(\eta) / \mathcal{F}_1(0)$ , where  $n_1 = \frac{\pi}{6} (\frac{kT}{\hbar v_F})^2$ ,  $\eta = E_F / kT$ ,  $\mathcal{F}_j(\eta)$  is the Fermi integral of order  $j$ ,  $E_F$  is the tunable Fermi level, and  $v_F$  is the Fermi velocity in graphene. We model different insulating substrates by using their appropriate values of the dielectric constants,  $\epsilon_s$ . Moreover, we take into account the modifications to the Fermi velocity,  $v_F$ , and dielectric constant of graphene,  $\epsilon_g$ , due to the substrate [12,44]. Suspended graphene is simulated by replacing the substrate by air.

We use the electronic tight-binding Bloch wave functions [45] to calculate the electron-phonon scattering rates in graphene based on Fermi's golden rule. As the scattering rates of electrons with out-of-plane phonons are several orders of magnitude lower than with in-plane modes [46], we neglect out-of-plane modes and compute the rates due to acoustic and optical in-plane phonon modes, accurately reproducing the rates from first-principles calculations [45–47]. For graphene on a substrate, we also calculate the electron-surface optical (SO) phonon scattering rates [48,49]. The values of parameters used in our simulations are shown in Table I. Electron interactions with ionized impurities and other carriers are not treated as additional scattering mechanisms, but accounted for dynamically, via the full-wave electromagnetic

TABLE I. Substrate parameters: Fermi velocity ( $v_F$ ), static dielectric constants of graphene ( $\epsilon_g$ ) and substrate ( $\epsilon_s$ ), high-frequency dielectric constant of substrate ( $\epsilon_s^\infty$ ), and SO phonon energy ( $\hbar\omega_{SO}$ ).

	SiO <sub>2</sub>	<i>h</i> -BN	Suspended
$v_F$ (m/s)	$1.1 \times 10^6$ [12]	$1.5 \times 10^6$ [12]	$1.5 \times 10^6$ [44]
$\epsilon_g$	2.45 [50]	3.04 [49]	4.9 [44]
$\epsilon_s$	3.9 [50]	5.09 [49]	1.0
$\epsilon_s^\infty$	2.5 [48]	4.1 [49]	
$\hbar\omega_{SO1}$ (meV)	59.98 [48]	101.42 [49]	
$\hbar\omega_{SO2}$ (meV)	146.51 [48]	195.83 [49]	

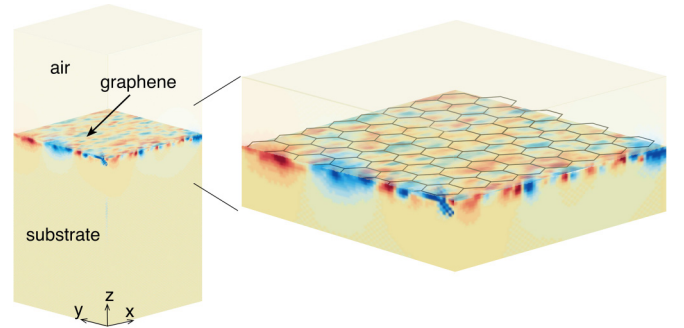


FIG. 1. (Color online) Schematic of the simulation domain (drawn to scale on the left), showing air, graphene, and a substrate. The colors near the graphene layer depict an example snapshot of the electric-field component along the in-plane  $x$  direction (blue: negative; red: positive) in the absence of external excitation. The field stems from the charge carriers (electrons and holes) and from clustered impurities located in the substrate within a few nanometers of the graphene sheet.

finite-difference time-domain and molecular dynamics (FDTD/MD) solver, which we describe in more detail in Sec. II B.

The simulation domain is depicted schematically in Fig. 1. We consider suspended graphene, as well as graphene on SiO<sub>2</sub> and on *h*-BN. In the simulation, the SiO<sub>2</sub> substrate is 300 nm thick, while for the *h*-BN substrate we consider a 10-nm-thick *h*-BN layer with a 290-nm-thick SiO<sub>2</sub> region underneath it, in order to mimic the typical structure used in experiments [11]. The planar dimensions of the simulation domain are chosen such that for a given carrier density there are at least 25 000 carriers in the domain; typically, the domain size is on the order of several hundred nanometers. The vertical boundary surfaces of the domain, perpendicular to the plane of graphene, are terminated with periodic boundary conditions in order to simulate a large graphene flake. The top and bottom boundary surfaces are terminated with perfectly matched absorbing boundary conditions [51]. We model charged substrate impurities down to a depth of 10 nm from the graphene layer by assuming a distribution of singly charged positive ions; impurities deeper than 10 nm have been shown to have a negligible effect on transport [43]. The clustered impurity distributions are generated to have a given average cluster size and a generally Gaussian autocorrelation function, as described in [43]. Throughout this paper, “clustered distribution” implies a distribution where the average cluster size is 45 nm; this cluster size has been shown to produce 20-nm-sized electron-hole puddles, as observed in experiment [43]. Figure 1 also shows an example of the in-plane electric-field distribution in the graphene layer without external illumination or biasing. The field stems from the thermal motion of carriers and the clustered charged impurities in the substrate.

We also note that scattering of electrons by resonant impurities, such as neutral organic molecules adsorbed to the surface of graphene [52], and by midgap states introduced by vacancy defects [53] has been previously discussed in regards to the sublinear dc conductivity of graphene. However, it has been shown that annealing, which decreases the number of adsorbed resonant impurities, results in higher sublinearity

[54]. Raman studies have shown that typical graphene samples have very few defects [55,56] and the formation energy of vacancies in graphene is fairly high (7.5 eV). We therefore do not account for resonant impurities or midgap states due to vacancies in this simulation.

### B. The EMC/FDTD/MD method

Our simulation combines diffusive carrier transport using the ensemble Monte Carlo (EMC) method [57] with an electrodynamics solver comprising the finite-difference time-domain (FDTD) method [51] and molecular dynamics (MD) [58]. The EMC, FDTD, and MD methods are coupled as follows. In EMC, which is a stochastic numerical technique that yields the solution to the Boltzmann transport equation, a large ensemble of carriers is tracked over time as they undergo scattering events and periods of free flight. The motion of carriers during free flight is governed by the Lorentz force arising from the local electromagnetic fields, which are calculated by using the FDTD solution to Maxwell's curl equations. An incident transverse electromagnetic plane wave of frequency  $f$  ( $\omega = 2\pi f$ ) and the current density arising from carrier motion in EMC act as field sources in FDTD; in turn, fields calculated by FDTD affect carrier motion in EMC. The current density is calculated from the carrier motion by using a combination of the cloud-in-cell method [59] of assigning charges to the grid and the Villasenor-Buneman method of computing current density in grid-based solvers [60]. Since grid-based techniques, such as FDTD, do not account for field variations on a length scale shorter than the grid-cell size, we use the MD method to calculate the sub-grid-cell short-range interactions among carriers (electrons and holes) and between carriers and impurity ions. We include carrier-ion and carrier-carrier interactions (direct and exchange) in MD. The complex conductivity is calculated from

$$\hat{\sigma}(\omega) = \frac{\hat{E}(\omega) \cdot \hat{J}(\omega)^*}{|\hat{E}(\omega)|^2}, \quad (1)$$

where  $\hat{J}(\omega)$  and  $\hat{E}(\omega)$  are the spatially averaged current-density and electric-field phasors, respectively.

For additional computational details on the EMC/FDTD/MD method, we refer the interested reader to Refs. [61,62]. The coupled EMC/FDTD/MD method has been successfully used for the simulation of high-frequency transport in bulk Si [37,61] and dc transport in graphene on SiO<sub>2</sub> with clustered impurities in the substrate [43,62].

As with any technique, there are limits of applicability of EMC/FDTD/MD. First, the transport kernel is semiclassical, so the technique cannot capture coherent transport features, which are important at very low temperatures or in very small structures. Second, the combined technique is limited to intraband transport and cannot describe interband absorption processes. For graphene, interband absorption becomes important at frequencies around  $2E_F/h$ ; for the carrier densities considered here ( $10^{12} - 10^{13} \text{ cm}^{-2}$ ), the Fermi energy is on the order of  $\sim 0.1 \text{ eV}$  (see, e.g., Fig. 4 in [45]). Therefore, for frequencies up to about 100 THz, only intraband transport in graphene is important, so the EMC/FDTD/MD technique reliably simulates transport and yields an accurate conductivity calculation.

## III. RESULTS AND DISCUSSION

### A. Matching experimental data

In Fig. 2(a), we show that the real part of  $\sigma(\omega)$  calculated by the EMC/FDTD/MD method reproduces experimental data with very good agreement. The impurity density  $N_i$  is the only variable parameter and a clustered impurity distribution is assumed. The solid lines are experimental results for graphene on SiO<sub>2</sub> at room temperature [blue: Ref. [33], UC Irvine (UCI) team; red: Ref. [38], UC Berkeley (UCB) team; black: Ref. [30], Rice University team]. The symbols (squares, triangles, and circles) represent our simulation results and the dashed lines are fits to the simulation data using the Drude model. We have assumed the same carrier densities as estimated in the experiments, which are  $n = 1.8 \times 10^{12} \text{ cm}^{-2}$  ([33], UCI),  $7.29 \times 10^{12} \text{ cm}^{-2}$  ([38], UCB), and  $7.74 \times 10^{12} \text{ cm}^{-2}$  ([30], Rice). The impurity densities that

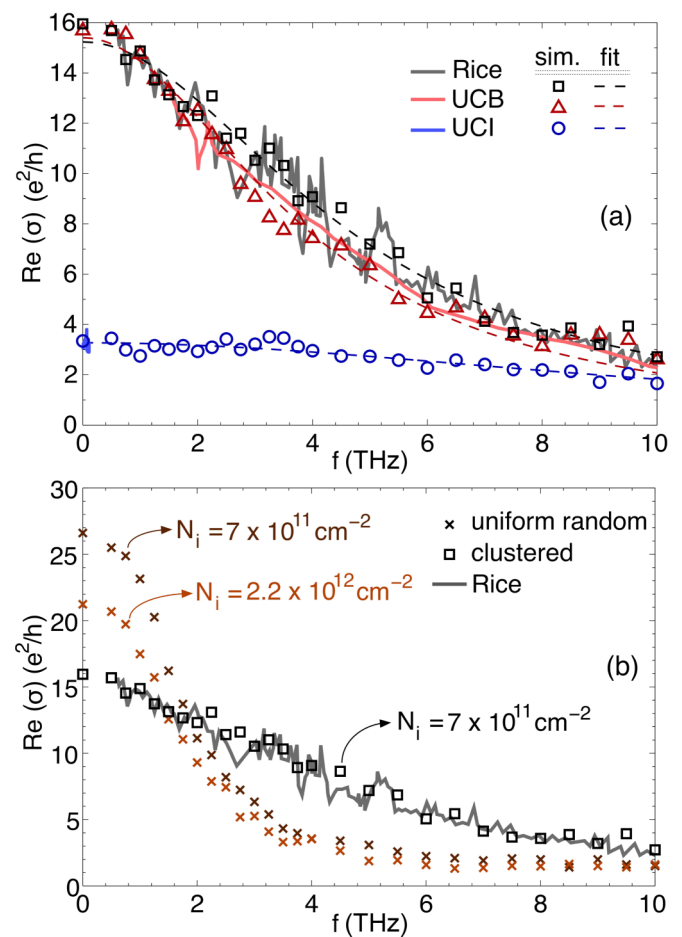


FIG. 2. (Color online) Real part of  $\sigma(\omega)$  as a function of frequency. (a) Calculated values based on the EMC/FDTD/MD simulation (squares, triangles, and circles) match, respectively, the experimental data from [33] (blue: UC Irvine), [38] (red: UC Berkeley), and [30] (black: Rice University). Dashed lines are Drude-model fits to the simulation data. (b) Calculated values with different types of impurity distributions, i.e., clustered (squares,  $N_i = 7 \times 10^{11} \text{ cm}^{-2}$ ) and uniform random (x symbols,  $N_i = 7 \times 10^{11} \text{ cm}^{-2}$  and  $N_i = 2.2 \times 10^{12} \text{ cm}^{-2}$ ), compared to the experimental data from the Rice group [30].

yield the best match to the experimental data of UCI, UCB, and Rice are, respectively,  $N_i = 5 \times 10^{11} \text{ cm}^{-2}$ ,  $8 \times 10^{11} \text{ cm}^{-2}$ , and  $7 \times 10^{11} \text{ cm}^{-2}$ . These impurity densities, providing an excellent agreement between the simulation and experimental data, are reasonable and quite likely in typical samples [63].

In Fig. 2(b), we compare the real part of  $\sigma(\omega)$  for clustered (squares) and uniform random (x symbols) impurity distributions with the experimental data from Rice University [30] (solid line). We demonstrate that with a uniform random distribution of impurities, we cannot obtain a good fit to experiment even with extremely high values of  $N_i$ , which presents further evidence that typical supported graphene samples contain clustered impurities [43]. For a given impurity density ( $N_i = 7 \times 10^{11} \text{ cm}^{-2}$ ), a uniform random impurity distribution results in higher conductivity at low frequencies ( $f < 2 \text{ THz}$ ) and lower conductivity at high frequencies than the clustered distribution. Our results with clustered charged impurities are contrary to the results presented in Ref. [26], in which Gaussian clusters of charged impurities were shown to enhance the conductivity with respect to a uniform random impurity distribution and clean graphene. The enhancement in conductivity was attributed to the emergence of states near the Dirac point that could lead to excitations between electron-hole puddles [26]. On the other hand, experiments have shown that clustered impurities lead to a reduction in the dc conductivity [64], which we have attributed to electrons/holes being trapped near the charged clusters [43]. Furthermore, from fitting the calculated frequency-dependent conductivity to the Drude model for the uniform random and clustered impurity distributions for the same  $N_i = 7 \times 10^{11} \text{ cm}^{-2}$ , we find that the effective scattering rate for the uniform random distribution ( $\Gamma = 2 \text{ THz}$ ) is much lower than that for the clustered distribution ( $\Gamma = 5 \text{ THz}$ ). The higher effective scattering rate for electrons with a clustered impurity distribution is expected, since the electrons trapped near the charged clusters scatter more frequently from the Coulomb potential.

### B. Drude vs generalized Drude model. Conductivity of suspended graphene

Next, we compare the frequency-dependent conductivity in supported and suspended graphene. In Fig. 3, we show the real part of  $\sigma(\omega)$  for suspended graphene (circles), graphene on *h*-BN (triangles), and graphene on SiO<sub>2</sub> (squares), all with the same electron density of  $6.3 \times 10^{12} \text{ cm}^{-2}$ . In the supported-graphene simulations, we account for clustered impurities with a sheet density of  $5 \times 10^{11} \text{ cm}^{-2}$ , while the suspended-graphene simulation is impurity free. The values of electron density and impurity density used here are typical in experiments [30,38,63]. It is clear from Fig. 3 that the substrate influences transport and a significant enhancement in the low-frequency THz conductivity can be obtained by suspending graphene.

For impurity-free suspended graphene, the simple Drude model (orange dashed line) does not yield a good fit in the frequency range considered here (see inset of Fig. 3). We obtain a better fit by using a generalized Drude model [36,37] (green solid line). The generalized Drude model is usually presented in terms of the static conductivity  $\sigma(0)$  and the

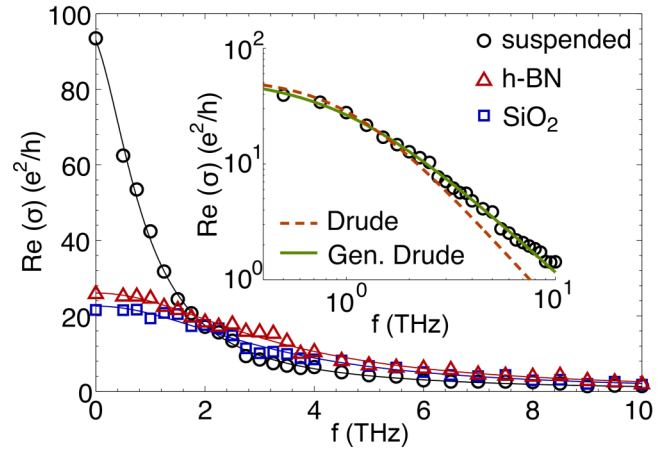


FIG. 3. (Color online) Real part of  $\sigma(\omega)$  for impurity-free suspended graphene (circle) and supported graphene with an impurity density of  $5 \times 10^{11} \text{ cm}^{-2}$  on *h*-BN (triangle) and SiO<sub>2</sub> (square). The electron density is  $6.3 \times 10^{12} \text{ cm}^{-2}$ . Inset: Comparison of the fits based on the simple Drude model and the generalized Drude model [Eq. (2)] to the calculated  $\sigma(\omega)$  for suspended graphene.

effective relaxation time  $\tau = \Gamma^{-1}$  [36]:

$$\sigma(\omega) = \frac{\sigma(0)}{[1 - (i\omega\tau)^{1-\alpha}]^\beta} = \frac{D}{\pi\Gamma[1 - (i\omega/\Gamma)^{1-\alpha}]^\beta}. \quad (2)$$

Here, we have introduced a generalized Drude weight via  $D = \pi\sigma(0)\Gamma$ , the same relationship that holds in the Drude model.  $\alpha$  and  $\beta$  are real-valued parameters ( $0 \leq \alpha, \beta \leq 1$ ). For  $\alpha = 0$  and  $\beta = 1$ , the generalized Drude model reduces to the simple Drude model, which assumes that energy-resolved carrier relaxation time is independent of energy, so a single value  $\tau$  describes the time response of the entire ensemble. This assumption is not realistic for semiconductors or for graphene, where electrons scatter with phonons, charged impurities, and other carriers, and the energy-resolved relaxation time can have a pronounced energy dependence [65]. With  $\alpha \neq 0$  and  $\beta \neq 1$ , the generalized Drude model allows for a continuum of relevant relaxation times, such that the distribution of the logarithms of relaxation times is peaked around the logarithm of the most prominent time,  $\tau = \Gamma^{-1}$  [66–68];  $\alpha$  indicates the peak width while  $\beta$  determines the symmetry of this distribution [36]. A number of well-known conductivity models for lossy dielectrics are special cases of the generalized Drude model; for example, the Cole-Cole model is obtained with  $\beta = 1$ , while the Cole-Davidson model corresponds to  $\alpha = 0$  [36].

In suspended graphene, the scattering mechanisms that directly affect conductivity are those between electrons and the intrinsic acoustic and optical phonons, and their rates are approximately linear in energy [45–47]. Therefore, the generalized Drude model is expected to yield a better fit than the Drude model. Figure 4 shows  $\Gamma$  and  $D$  in suspended graphene as a function of carrier density, with (circles) and without (triangles) the short-range electron-electron interaction captured via MD. Both  $\Gamma$  and  $D$  show a slight reduction due to the short-range electron-electron interactions at high  $n$ . The best-generalized-Drude-fit values for  $\alpha$  and  $\beta$  are given in the inset to Fig. 4(a) as a function of carrier

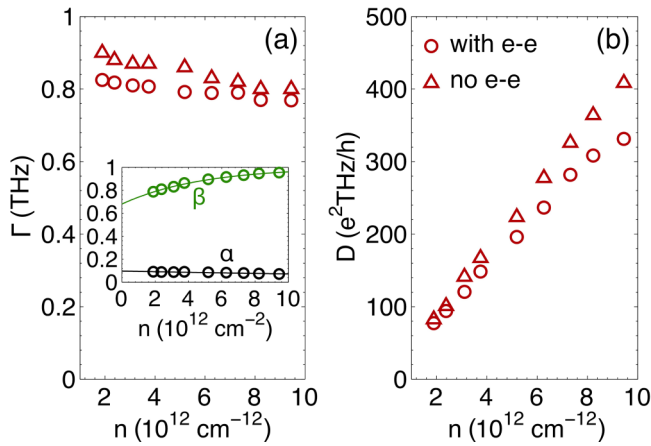


FIG. 4. (Color online) (a) The effective relaxation rate  $\Gamma$  and (b) Drude weight  $D$  for suspended graphene as functions of the electron density  $n$ , obtained from a generalized-Drude-model fit [Eq. (2)] to the simulation results. Circles (triangles) correspond to the short-range electron-electron interaction included in (excluded from) the simulation. Inset: Parameters  $\alpha$  (black open circles) and  $\beta$  (green open circles), corresponding to the best-generalized-Drude-model fits to the simulation results [Eq. (2)], presented as a function of  $n$ . Curves are  $\alpha(n) = 0.097 \exp(-0.03n)$  (black solid curve) and  $\beta(n) = 1 - 0.32 \exp(-0.21n)$  (green solid curve), where  $n$  is in  $10^{12} \text{ cm}^{-2}$ .

density. These dependencies approximately follow  $\alpha(n) = 0.097 \exp(-0.03n)$  and  $\beta(n) = 1 - 0.32 \exp(-0.21n)$ , where  $n$  is in  $10^{12} \text{ cm}^{-2}$  [we sought forms that reduce to the simple Drude model for very high  $n$ , i.e.,  $\alpha(\infty) = 0$  and  $\beta(\infty) = 1$ ]. While  $\alpha$  is uniformly small, indicating that the distribution of relaxation-time logarithms is sharply peaked around its value at  $\Gamma^{-1}$ , there is a notable increase in  $\beta$  with increasing  $n$ , which indicates a transition from a fairly asymmetric to fairly symmetric distribution of relaxation-time logarithms, in agreement with moving from electron-phonon to electron-electron interactions as dominant.

For supported graphene, where the SO phonons and charged impurities scatter electrons in addition to the intrinsic graphene phonons, we obtain  $\alpha$  and  $\beta$  very close to the Drude-model values of 0 and 1, respectively. These values hold for both  $\text{SiO}_2$  and  $h\text{-BN}$  substrates. They indicate that the mechanism with an approximately energy-independent scattering rate dominates transport in supported graphene, which is the electron-charged impurity scattering [39,41]. Although the simple Drude model provides a very good fit to the supported graphene  $\sigma(\omega)$ , we fit all the data in Fig. 3 (and all subsequent  $\sigma$  vs  $f$  plots) with the generalized Drude model [Eq. (2)], while recognizing that for supported systems the generalized and simple Drude models essentially coincide.

### C. Effective scattering rate for supported graphene

We examine the dependence of  $\sigma(\omega)$  on the impurity density in Fig. 5(a). We show the real part of  $\sigma(\omega)$  in graphene supported on  $\text{SiO}_2$  (filled symbols) and  $h\text{-BN}$  (open symbols), while accounting for clustered impurities with different sheet impurity densities [ $N_i = 10^{11} \text{ cm}^{-2}$  (circles),  $5 \times 10^{11} \text{ cm}^{-2}$  (triangles),  $10^{12} \text{ cm}^{-2}$  (squares)]. The electron density is fixed at  $n = 3.75 \times 10^{12} \text{ cm}^{-2}$ . We find that the substrate plays

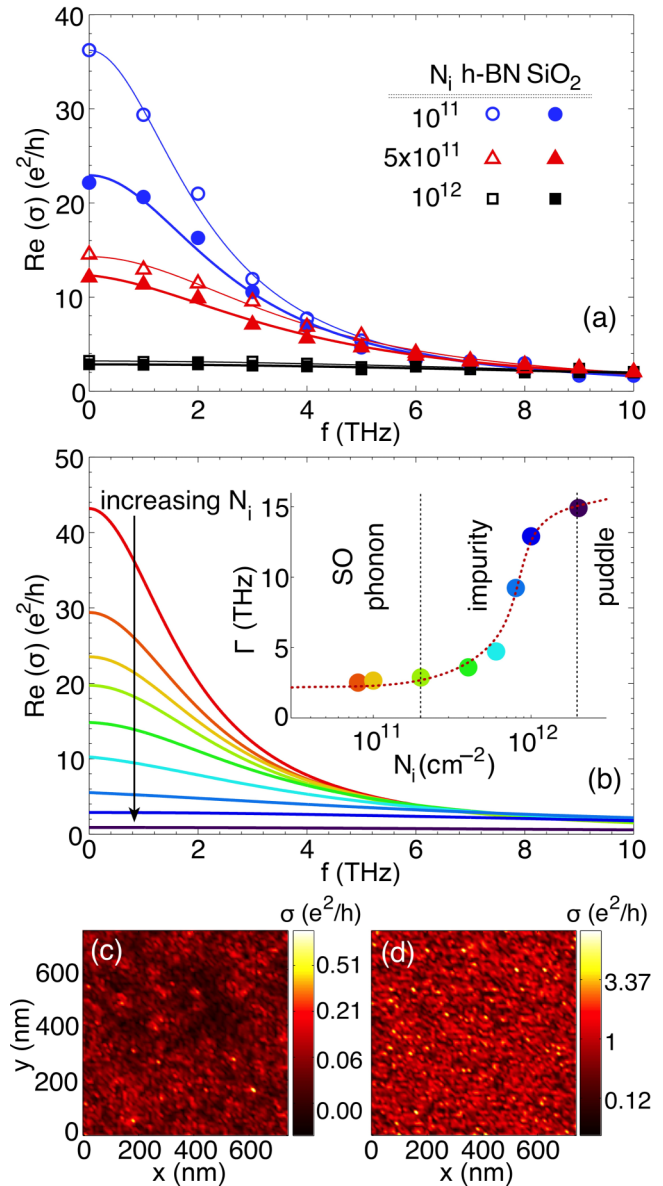


FIG. 5. (Color online) (a) Real part of  $\sigma(\omega)$  for graphene supported on  $\text{SiO}_2$  (solid symbols) and  $h\text{-BN}$  (open symbols) for different  $N_i$  (circles:  $7 \times 10^{11} \text{ cm}^{-2}$ ; triangles:  $5 \times 10^{11} \text{ cm}^{-2}$ ; squares:  $10^{12} \text{ cm}^{-2}$ ), with an electron density of  $n = 3.75 \times 10^{12} \text{ cm}^{-2}$ . (b) Generalized-Drude-model best fits to the calculated  $\sigma(\omega)$  for graphene on  $\text{SiO}_2$  with different impurity densities, from top (red) to bottom (purple):  $N_i = 0, 8 \times 10^{10}, 10^{11}, 2 \times 10^{11}, 4 \times 10^{11}, 6 \times 10^{11}, 8 \times 10^{11}, 10^{12}$ , and  $2 \times 10^{12} \text{ cm}^{-2}$ . Inset:  $\Gamma$  corresponding to the generalized-Drude-model fits in the main panel as a function of  $N_i$ . Circle colors in the inset correspond to the curve colors in the main panel. (c),(d) Local conductance maps at a frequency of 2 THz for graphene on  $\text{SiO}_2$  with a clustered impurity density of (c)  $N_i = 2 \times 10^{12} \text{ cm}^{-2}$  and (d)  $N_i = 8 \times 10^{10} \text{ cm}^{-2}$ .

an important role in transport at low frequencies and low impurity densities. When the impurity density approaches the electron density ( $N_i = 10^{12} \text{ cm}^{-2}$ ), conductivity is low for both substrates and over all frequencies. These results shed light on the factors influencing conductivity. Intuitively, as long as the frequency is low enough that an electron can

complete several scattering events during a period of the field, transport is qualitatively the same as in the static case, with different substrates and different impurity densities resulting in different  $\sigma(\omega)$ . However, once the frequency becomes high enough that an electron cannot traverse the average distance between scattering centers (the mean free path,  $l_{\text{mfp}}$ ) within a time on the order of one electromagnetic field period, i.e., when  $f \gtrsim v_F/l_{\text{mfp}}$ , the diffusive transport picture is disturbed and the ability of the electron to participate in the current flow is reduced; the field effectively helps localize the electron. At low impurity densities, the static conductivity is appreciable,  $l_{\text{mfp}}$  is long, and the variation of conductivity with frequency is pronounced. With increasing impurity density,  $l_{\text{mfp}}$  decreases and the frequency at which the conductivity rapidly falls off increases; however, dc conductivity drops, as well, and the range over which  $\sigma$  varies shrinks. The difference between SiO<sub>2</sub> and *h*-BN is pronounced only at low impurity densities and at low frequencies, as expected. Either a high impurity density or a high frequency overshadows the benefits of the *h*-BN substrate over SiO<sub>2</sub>. For typical sheet impurity densities, we can resolve  $\sigma$  by impurity density and substrate type up to frequencies of about 4 THz.

In Fig. 5(b), we look more closely at the effective scattering rate  $\Gamma$ . In the main panel, we show  $\text{Re}(\sigma)$  from the best generalized-Drude fits [Eq. (2)] to our simulation data for graphene on SiO<sub>2</sub>. Different curves correspond to different  $N_i$ : from top (red) to bottom (purple),  $N_i = 0, 8 \times 10^{10}, 10^{11}, 2 \times 10^{11}, 4 \times 10^{11}, 6 \times 10^{11}, 8 \times 10^{11}, 10^{12}$ , and  $2 \times 10^{12} \text{ cm}^{-2}$ . The electron density is the same as for Fig. 5(a),  $n = 3.75 \times 10^{12} \text{ cm}^{-2}$ . From the fits, we have obtained  $\Gamma$  as a function of  $N_i$ , shown in the inset to Fig. 5(b); the colors of the filled circles in the inset correspond to those of the lines in the main panel. At low sheet impurity densities ( $N_i/n \lesssim 0.1$ ), the electron distribution is nearly uniform and electron-SO phonon scattering governs transport, which can be seen from the nearly constant effective scattering rate as a function of  $N_i$ . With increasing impurity density, the total effective scattering rate increases rapidly due to an increase in the electron-charged impurity scattering. As the impurity density approaches the electron density ( $N_i/n \gtrsim 0.5$ ), the electron distribution becomes inhomogeneous: electron-hole puddles form [42,69] as the carriers effectively get trapped in the vicinity of the impurity clusters [43]. In the transport regime dominated by electron-hole puddles, any further increase in the impurity density does not have a significant effect on transport, as seen from the saturation of  $\Gamma$ . We indicate these different transport regimes as SO-phonon dominated, impurity dominated, and puddle dominated in the inset of Fig. 5(b). A quick back-of-the-envelope calculation with  $v_F \approx 10^6 \text{ m/s}$  and  $\Gamma = 15 \text{ THz}$  shows that the mean free path in this regime is on the order of the cluster size, i.e.,  $l_{\text{mfp}} = v_F/\Gamma \approx 67 \text{ nm}$ .

The puddle-dominated transport regime can be discerned from the local conductance map of graphene on SiO<sub>2</sub> for  $N_i = 2 \times 10^{12} \text{ cm}^{-2}$ , shown in Fig. 5(c). By comparison, for  $N_i = 8 \times 10^{10} \text{ cm}^{-2}$ , shown in Fig. 5(d), the local conductance is fairly uniform. Both of these conductance maps are computed at 2 THz, a frequency low enough to show diffusive transport details. As before, the local conductance is calculated using Eq. (1), except that the phasor quantities ( $\hat{J}$  and  $\hat{E}$ ) are now not spatially averaged. Local conductance

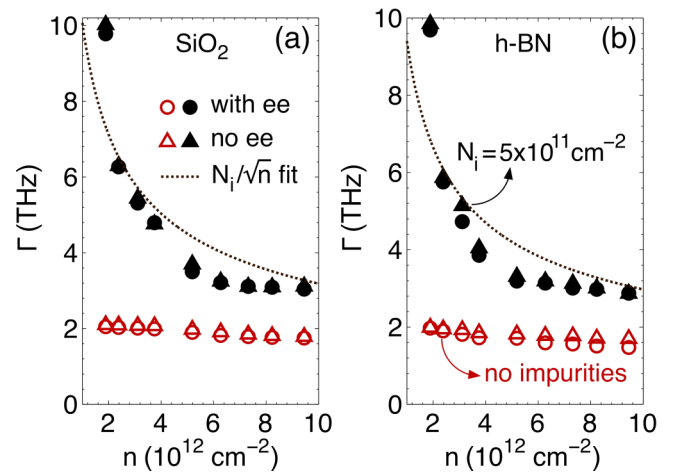


FIG. 6. (Color online) The effective scattering rate  $\Gamma$  as a function of the electron density  $n$ , obtained from a generalized-Drude-model fit [Eq. (2)] to the simulation results for graphene supported on (a) SiO<sub>2</sub> and (b) *h*-BN, with and without impurities. The best fit for supported graphene is achieved with parameters  $\alpha \approx 0$  and  $\beta \approx 1$ , yielding the simple Drude model. Open red symbols correspond to the results without impurities, while the solid black symbols denote the inclusion of impurities with  $N_i = 5 \times 10^{11} \text{ cm}^{-2}$ . Circles (triangles) correspond to the electron-electron interaction included (excluded) in the simulation. The dotted line represents the  $\sim N_i/\sqrt{n}$  dependence.

maps obtained experimentally through a combination of a micro four-point probe and THz time-domain spectroscopy [70] are qualitatively similar to our simulation results, shown in Fig. 5(c), thus providing further evidence for the predominance of clustered impurity distributions in typical samples.

In Figs. 6(a) and 6(b), we show the effective scattering rate as a function of carrier density for graphene on SiO<sub>2</sub> and *h*-BN. We examine the effects of electron-electron and electron-charged impurity interactions by selectively turning on (circles) and off (triangles) the short-range electron-electron direct and exchange interactions in MD, and by simulating transport with (solid black symbols) and without (open red symbols) impurities. In the simulations with impurities, we use an impurity sheet density of  $5 \times 10^{11} \text{ cm}^{-2}$ . The influence of electron-charged impurity scattering and screening is evident from the sharp drop in  $\Gamma(n)$  as the screening of the impurities becomes more effective with increasing  $n$ . Short-range electron-electron interactions and the substrate SO phonons, on the other hand, influence  $\Gamma(n)$  very weakly. Moreover, we show that a curve of the form  $\sim N_i/\sqrt{n}$ , which is shown by the dotted lines in Figs. 6(a) and 6(b) and is the expected dependence for the electron-impurity scattering rate when a sheet of uniformly distributed charged impurities is at a certain distance from graphene [39,40], does not fit the  $\Gamma(n)$  data obtained from our simulations. The discrepancy likely comes from the more realistic, volumetric distributions of impurities considered here.

Recent experiments, where the effective scattering rate was extracted from Drude-model fits to  $\sigma(\omega)$ , have shown  $\Gamma(n)$  to be either nearly constant (hole regime) or to increase linearly with  $n$  (electron regime) [31]. The nearly constant  $\Gamma(n)$  would

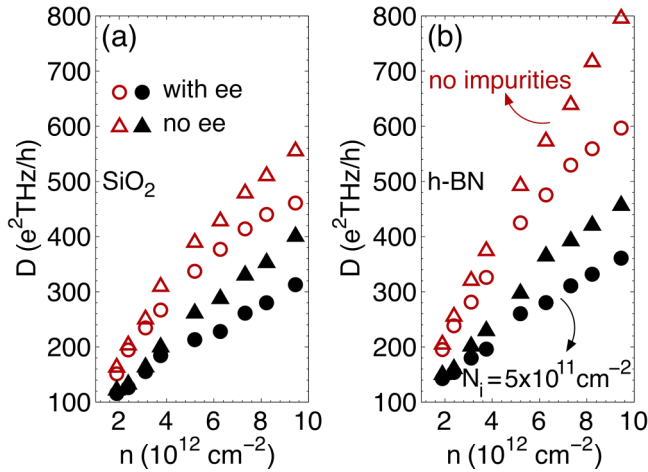


FIG. 7. (Color online) The Drude weight  $D$  as a function of the electron density  $n$ , obtained from a generalized-Drude-model fit [Eq. (2)] to the simulation results for graphene supported on (a)  $\text{SiO}_2$  and (b)  $h\text{-BN}$ , with and without impurities. The best fit for supported graphene is achieved with parameters  $\alpha \approx 0$  and  $\beta \approx 1$ , yielding the simple Drude model. Open red symbols correspond to the results without impurities, while the solid black symbols denote the inclusion of impurities with  $N_i = 5 \times 10^{11} \text{cm}^{-2}$ . Circles (triangles) correspond to the electron-electron interaction included in (excluded from) the simulation.

represent transport in a regime where carrier-phonon scattering dominates; however, the linear increase in  $\Gamma(n)$  cannot be explained from our simulation results presented here, even when impurities with the same sign of charge as the carriers are considered. The asymmetry in the hole and electron regimes in the results from Ref. [31] likely suggests Fermi-level pinning or extrinsic doping from the metal/graphene interface at the contacts [71].

#### D. Drude weight for supported graphene

In Fig. 7, we show the Drude weight as a function of the electron density,  $D(n)$ , obtained from a generalized-Drude-model fit to our simulation results for graphene on  $\text{SiO}_2$  and on  $h\text{-BN}$ . Here, the symbols represent the same conditions as in Fig. 6, i.e., the results with (without) short-range electron-electron interactions are shown with circles (triangles), while the results with (without) impurities are shown with solid black (open red) symbols. It is clear that both charged impurities and electron-electron interactions lead to a reduction of  $D$ . The substrate also affects the Drude weight, with the  $h\text{-BN}$  substrate resulting in the highest Drude weight for a given electron density. Turning the short-range electron-electron interaction on results in a 5–25% decrease in  $D$ . However, when we compare the data with and without impurities, we see that including the electron-impurity interactions (for  $N_i = 5 \times 10^{11} \text{cm}^{-2}$ ) leads to a 25–40% reduction in  $D$  with respect to the impurity-free value on each substrate, a percentage close to that determined from experiment [31]. A significant variation in the reduction of  $D$  from sample to sample observed in Ref. [35] also points towards charged impurities as the dominant factor affecting  $D$ .

Previous theoretical calculations that included electron-electron interactions via a first-order calculation predicted an enhancement in  $D$ , weakly dependent on  $n$ , with respect to the RPA value  $D_0$  [22]. We stress that, in this paper, what we turn on or off is *only the short-range portion* of the electron-electron interaction, captured by MD. The long-range Hartree terms of the electron-electron interaction are always present in the calculation; they are captured by the FDTD solver. (We do not expect correlation effects to play an important role at room temperature and for the electron densities considered here [72].)

The reason behind the decrease in  $D$  with the inclusion of short-range electron-electron interactions is somewhat subtle. Basically, the Drude weight is proportional to the product of the static conductivity  $\sigma(0)$  and the effective scattering rate  $\Gamma$ .  $\Gamma$  is fairly insensitive to the inclusion of the short-range electron-electron interactions, which means that the screening of dominant interactions (with impurities and substrate phonons) appears to be well-captured by the long-range fields that FDTD calculates. However,  $\sigma(0)$  displays a marked drop with the inclusion of short-range electron-electron interactions [43]: with short-range electron-electron interactions, the single-electron distribution over energy is broader than without them, so higher-energy states are populated. As a result, the ensemble-averaged scattering rate with phonons will also be higher because the energy-resolved scattering rate is proportional to the electron density of states, thus nearly linear in energy for graphene [45,47]. Electron-phonon scattering is very efficient at randomizing momentum, so while its contribution to  $\Gamma$  may not be very high (especially in the presence of high impurity densities), its relative contribution to  $\sigma(0)$  is considerable because all other interactions are Coulomb in origin and result in small-angle scattering and thus a small relative contribution to  $\sigma(0)$ . Therefore,  $D$  drops

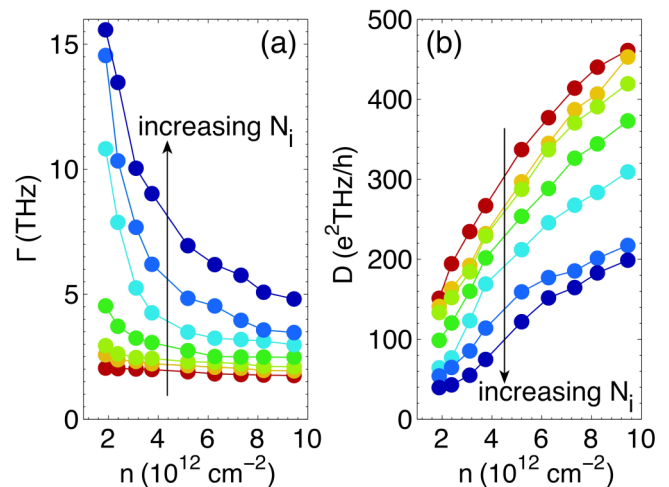


FIG. 8. (Color online) (a) The effective scattering rate  $\Gamma$  and (b) Drude weight  $D$  as a function of the electron density  $n$ , obtained from a generalized-Drude-model fit [Eq. (2)] to the simulation results for graphene supported on  $\text{SiO}_2$  with different impurity densities. The color scheme is the same as in Fig. 5, with colors from red to blue corresponding to  $N_i = 0, 10^{11}, 2 \times 10^{11}, 4 \times 10^{11}, 6 \times 10^{11}, 8 \times 10^{11}$ , and  $10^{12} \text{cm}^{-2}$ . The color- $N_i$  correspondence is the same as in Fig. 5.

when short-range electron-electron interactions are included for the same reason  $\sigma(0)$  drops [43], which is an indirect enhancement of the effective momentum relaxation rate with phonons owing to the electron redistribution over energy.

Finally, in Fig. 8, we show  $\Gamma$  and  $D$  for graphene on SiO<sub>2</sub> as a function of carrier density, for different values of the substrate impurity density. Based on Fig. 8 and the  $\Gamma$  and  $D$  values obtained from the measured  $\sigma(\omega)$ , one can estimate the sheet impurity density in experiment.

#### IV. CONCLUSION

In summary, we have presented a detailed study of the frequency-dependent conductivity in the THz range at room temperature in supported and suspended graphene for a wide range of electron and impurity densities. We have employed a self-consistent simulation that couples electron transport via EMC with a full-wave electrodynamics solver that comprises the FDTD method and MD. We have examined the effects of charged impurities, the underlying substrate, and electron-electron interactions on the effective scattering rate and the Drude weight, which are obtained by fitting the generalized Drude model to the numerically calculated  $\sigma(\omega)$  for graphene on SiO<sub>2</sub> and *h*-BN, and for suspended graphene.

We find an excellent agreement between the experimental data for  $\sigma(\omega)$  [30,33,38] and the simulation, with clustered impurities and the sheet impurity density as the only variable parameter. Our results indicate that electron-charged impurity scattering dominates the carrier dynamics in supported graphene, which manifests itself in the good fit of the  $\sigma(\omega)$  curves by the simple Drude model. In contrast, a generalized-Drude model is required to obtain a good fit for  $\sigma(\omega)$  in suspended graphene. The effects of the substrate, namely the

different electron-SO phonon scattering rates [48,49] and the modified Fermi velocity [12,44], are important only at low frequencies (<4 THz) and low impurity densities ( $N_i/n < 0.1$ ). These are important constraints for the effectiveness of substrate engineering [11,12] as a means to modify the electronic properties of graphene. With increasing sheet impurity density ( $0.1 < N_i/n < 0.5$ ), the effective scattering rate increases rapidly with  $N_i$  and then saturates at higher values of the impurity density ( $N_i/n > 0.5$ ), where transport is completely dominated by the electron-hole puddles.

Furthermore, by selectively turning off the short-range interparticle interactions in MD, we show that the effective scattering rate is nearly unaffected by electron-electron interactions. On the other hand, both electron-electron and electron-impurity interactions lead to a reduction in the Drude weight. The reduction in  $D$  due to electron-electron interactions varies between 5–25%, while that due to electron-impurity scattering varies between 25–40% (for  $N_i = 5 \times 10^{11} \text{ cm}^{-2}$ ). The substrate also affects the Drude weight: without impurities, graphene on *h*-BN has a higher Drude weight for a given electron density than either graphene on SiO<sub>2</sub> or suspended graphene.

In conclusion, a combination of substrate engineering (such as using thin films of *h*-BN on SiO<sub>2</sub>) with impurity density reduction could lead to a notable enhancement in  $\sigma(\omega)$  and  $D$ , which would benefit the applications of graphene at THz frequencies.

#### ACKNOWLEDGMENTS

This work has been primarily supported by AFOSR, Award No. FA9550-11-1-0299. Partial support by the U.S. Department of Energy, Award No. DE-SC0008712, is also acknowledged.

- 
- [1] A. S. Mayorov, R. V. Gorbachev, S. V. Morozov, L. Britnell, R. Jalil, L. A. Ponomarenko, P. Blake, K. S. Novoselov, K. Watanabe, T. Taniguchi, and A. K. Geim, *Nano Lett.* **11**, 2396 (2011).
  - [2] K. I. Bolotin, K. Sikes, Z. Jiang, M. Klima, G. Fudenberg, J. Hone, P. Kim, and H. Stormer, *Solid State Commun.* **146**, 351 (2008).
  - [3] K. S. Novoselov, A. K. Geim, S. V. Morozov, D. Jiang, Y. Zhang, S. V. Dubonos, I. V. Grigorieva, and A. A. Firsov, *Science* **306**, 666 (2004).
  - [4] S. Das Sarma, S. Adam, E. Hwang, and E. Rossi, *Rev. Mod. Phys.* **83**, 407 (2011).
  - [5] P. Avouris, *Nano Lett.* **10**, 4285 (2010).
  - [6] F. Schwierz, *Nat. Nano* **5**, 487 (2010).
  - [7] F. Bonaccorso, Z. Sun, T. Hasan, and A. C. Ferrari, *Nat. Photon.* **4**, 611 (2010).
  - [8] T. Otsuji, S. A. B. Tombet, A. Satou, H. Fukidome, M. Suemitsu, E. Sano, V. Popov, M. Ryzhii, and V. Ryzhii, *J. Phys. D: Appl. Phys.* **45**, 303001 (2012).
  - [9] M. Pumera, *Mater. Today* **14**, 308 (2011).
  - [10] L. G. P. Martins, Y. Song, T. Zeng, M. S. Dresselhaus, J. Kong, and P. T. Araujo, *Proc. Natl. Acad. Sci. USA* **110**, 17762 (2013).
  - [11] C. R. Dean, A. F. Young, I. Meric, C. Lee, L. Wang, S. Sorgenfrei, K. Watanabe, T. Taniguchi, P. Kim, K. L. Shepard, and J. Hone, *Nat. Nanotechnol.* **5**, 722 (2010).
  - [12] C. Hwang, D. A. Siegel, S.-K. Mo, W. Regan, A. Ismach, Y. Zhang, A. Zettl, and A. Lanzara, *Sci. Rep.* **2**, 590 (2012).
  - [13] M. Jablan, H. Buljan, and M. Soljačić, *Phys. Rev. B* **80**, 245435 (2009).
  - [14] F. H. L. Koppens, D. E. Chang, and F. J. García de Abajo, *Nano Lett.* **11**, 3370 (2011).
  - [15] H. Yan, T. Low, W. Zhu, Y. Wu, M. Freitag, X. Li, F. Guinea, P. Avouris, and F. Xia, *Nat. Photon.* **7**, 394 (2013).
  - [16] A. N. Grigorenko, M. Polini, and K. S. Novoselov, *Nat. Photon.* **6**, 749 (2012).
  - [17] T. Stauber, *J. Phys.: Condens. Matter* **26**, 123201 (2014).
  - [18] B. Sensale-Rodriguez, R. Yan, M. M. Kelly, T. Fang, K. Tahy, W. S. Hwang, D. Jena, L. Liu, and H. G. Xing, *Nat. Commun.* **3**, 780 (2012).
  - [19] S. A. Mikhailov, *Phys. Rev. B* **87**, 115405 (2013).
  - [20] H. Wang, A. Hsu, and T. Palacios, *IEEE Microwave Mag.* **13**, 114 (2012).
  - [21] P. Tassin, T. Koschny, M. Kafesaki, and C. M. Soukoulis, *Nat. Photon.* **6**, 259 (2012).

- [22] S. H. Abedinpour, G. Vignale, A. Principi, M. Polini, W.-K. Tse, and A. H. MacDonald, *Phys. Rev. B* **84**, 045429 (2011).
- [23] E. G. Mishchenko, *Phys. Rev. Lett.* **98**, 216801 (2007).
- [24] T. Stauber, N. M. R. Peres, and A. K. Geim, *Phys. Rev. B* **78**, 085432 (2008).
- [25] S. Y. Liu, N. Horing, and X. L. Lei, *IEEE Sens. J.* **10**, 681 (2010).
- [26] S. Yuan, R. Roldán, H. De Raedt, and M. I. Katsnelson, *Phys. Rev. B* **84**, 195418 (2011).
- [27] N. M. R. Peres, T. Stauber, and A. H. C. Neto, *Europhys. Lett.* **84**, 38002 (2008).
- [28] F. T. Vasko, V. V. Mitin, V. Ryzhii, and T. Otsuji, *Phys. Rev. B* **86**, 235424 (2012).
- [29] Z. Q. Li, E. A. Henriksen, Z. Jiang, Z. Hao, M. C. Martin, P. Kim, H. L. Stormer, and D. N. Basov, *Nat. Phys.* **4**, 532 (2008).
- [30] L. Ren, Q. Zhang, J. Yao, Z. Sun, R. Kaneko, Z. Yan, S. Nanot, Z. Jin, I. Kawayama, M. Tonouchi, J. M. Tour, and J. Kono, *Nano Lett.* **12**, 3711 (2012).
- [31] J. Horng, C.-F. Chen, B. Geng, C. Girit, Y. Zhang, Z. Hao, H. A. Bechtel, M. Martin, A. Zettl, M. F. Crommie, Y. R. Shen, and F. Wang, *Phys. Rev. B* **83**, 165113 (2011).
- [32] J. M. Dawlaty, S. Shivaraman, J. Strait, P. George, M. Chandrashekar, F. Rana, M. G. Spencer, D. Veksler, and Y. Chen, *Appl. Phys. Lett.* **93**, 131905 (2008).
- [33] N. Rouhi, S. Capdevila, D. Jain, K. Zand, Y. Wang, E. Brown, L. Jofre, and P. Burke, *Nano Res.* **5**, 667 (2012).
- [34] H. Choi, F. Borondics, D. A. Siegel, S. Y. Zhou, M. C. Martin, A. Lanzara, and R. A. Kaindl, *Appl. Phys. Lett.* **94**, 172102 (2009).
- [35] H. Yan, F. Xia, W. Zhu, M. Freitag, C. Dimitrakopoulos, A. A. Bol, G. Tulevski, and P. Avouris, *ACS Nano* **5**, 9854 (2011).
- [36] M. C. Beard, G. M. Turner, and C. A. Schmuttenmaer, *Phys. Rev. B* **62**, 15764 (2000).
- [37] K. J. Willis, S. C. Hagness, and I. Knezevic, *Appl. Phys. Lett.* **102**, 122113 (2013).
- [38] L. Ju, B. Geng, J. Horng, C. Girit, M. Martin, Z. Hao, H. A. Bechtel, X. Liang, A. Zettl, Y. R. Shen, and F. Wang, *Nat. Nanotechnol.* **6**, 630 (2011).
- [39] T. Ando, *J. Phys. Soc. Japan* **75**, 074716 (2006).
- [40] E. H. Hwang and S. Das Sarma, *Phys. Rev. B* **77**, 195412 (2008).
- [41] S. Adam, E. H. Hwang, V. M. Galitski, and S. Das Sarma, *Proc. Natl. Acad. Sci USA* **104**, 18392 (2007).
- [42] E. Rossi and S. Das Sarma, *Phys. Rev. Lett.* **101**, 166803 (2008).
- [43] N. Sule, S. C. Hagness, and I. Knezevic, *Phys. Rev. B* **89**, 165402 (2014).
- [44] D. C. Elias, R. V. Gorbachev, A. S. Mayorov, S. V. Morozov, A. A. Zhukov, P. Blake, L. A. Ponomarenko, I. V. Grigorieva, K. S. Novoselov, F. Guinea, and A. K. Geim, *Nat. Phys.* **8**, 172 (2012).
- [45] N. Sule and I. Knezevic, *J. Appl. Phys.* **112**, 053702 (2012).
- [46] K. M. Borysenko, J. T. Mullen, E. A. Barry, S. Paul, Y. G. Semenov, J. M. Zavada, M. B. Nardelli, and K. W. Kim, *Phys. Rev. B* **81**, 121412 (2010).
- [47] M. V. Fischetti, J. Kim, S. Narayanan, Z.-Y. Ong, C. Sachs, D. K. Ferry, and S. J. Aboud, *J. Phys.: Condens. Matter* **25**, 473202 (2013).
- [48] A. Konar, T. Fang, and D. Jena, *Phys. Rev. B* **82**, 115452 (2010).
- [49] I.-T. Lin and J.-M. Liu, *Appl. Phys. Lett.* **103**, 081606 (2013).
- [50] K. R. Knox, S. Wang, A. Morgante, D. Cvetko, A. Locatelli, T. O. Mendes, M. A. Niño, P. Kim, and R. M. Osgood, *Phys. Rev. B* **78**, 201408 (2008).
- [51] A. Taflove and S. Hagness, *Computational Electrodynamics: The Finite-Difference Time-Domain Method* (Artech, Norwood, MA, 2005).
- [52] T. O. Wehling, S. Yuan, A. I. Lichtenstein, A. K. Geim, and M. I. Katsnelson, *Phys. Rev. Lett.* **105**, 056802 (2010).
- [53] T. Stauber, N. M. R. Peres, and F. Guinea, *Phys. Rev. B* **76**, 205423 (2007).
- [54] K. I. Bolotin, K. J. Sikes, J. Hone, H. L. Stormer, and P. Kim, *Phys. Rev. Lett.* **101**, 096802 (2008).
- [55] D. Graf, F. Molitor, K. Ensslin, C. Stampfer, A. Jungen, C. Hierold, and L. Wirtz, *Nano Lett.* **7**, 238 (2007).
- [56] F. Banhart, J. Kotakoski, and A. V. Krasheninnikov, *ACS Nano* **5**, 26 (2011).
- [57] C. Jacoboni and L. Reggiani, *Rev. Mod. Phys.* **55**, 645 (1983).
- [58] D. Rapaport, *The Art of Molecular Dynamics Simulation* (Cambridge University Press, Cambridge, UK, 2004).
- [59] S. Laux, *IEEE Trans. Comput-Aided Des. Integr. Circuits Syst.* **15**, 1266 (1996).
- [60] J. Villasenor and O. Buneman, *Comput. Phys. Commun.* **69**, 306 (1992).
- [61] K. J. Willis, S. C. Hagness, and I. Knezevic, *J. Appl. Phys.* **110**, 063714 (2011).
- [62] N. Sule, K. J. Willis, S. C. Hagness, and I. Knezevic, *J. Comput. Electron.* **12**, 563 (2013).
- [63] Y.-W. Tan, Y. Zhang, K. Bolotin, Y. Zhao, S. Adam, E. H. Hwang, S. Das Sarma, H. L. Stormer, and P. Kim, *Phys. Rev. Lett.* **99**, 246803 (2007).
- [64] J. Yan and M. S. Fuhrer, *Phys. Rev. Lett.* **107**, 206601 (2011).
- [65] M. Lundstrom, *Fundamentals of Carrier Transport*, 2nd ed. (Cambridge University Press, Cambridge, UK, 2000).
- [66] K. W. Wagner, *Ann. Phys.* **345**, 817 (1913).
- [67] W. A. Yager, *J. Appl. Phys.* **7**, 434 (1936).
- [68] R. M. Hill and L. A. Dissado, *J. Phys. C* **18**, 3829 (1985).
- [69] Y. Zhang, V. W. Brar, C. Girit, A. Zettl, and M. F. Crommie, *Nat. Phys.* **5**, 722 (2009).
- [70] J. D. Buron, D. H. Petersen, P. Bøggild, D. G. Cooke, M. Hilke, J. Sun, E. Whiteway, P. F. Nielsen, O. Hansen, A. Yurgens, and P. U. Jepsen, *Nano Lett.* **12**, 5074 (2012).
- [71] B. Huard, N. Stander, J. A. Sulpizio, and D. Goldhaber-Gordon, *Phys. Rev. B* **78**, 121402 (2008).
- [72] J. Martin, N. Akerman, G. Ulbricht, T. Lohmann, J. H. Smet, K. von Klitzing, and A. Yacoby, *Nat. Phys.* **4**, 144 (2008).